Research Article Vol. 12, No. 12 / December 2024 / Photonics Research 2919

PHOTONICS Research

Observation of spatiotemporal dynamics for topological surface states with on-demand dispersion

Zhanyuan Zhang,[1,†] Zhihao Lan,[2,†] Pengbai Xu,[1,3] Leiming Wu,[1,3] Menglin L. N. Chen,[4] Wei E. I. Sha,[5] Yi Xu,[1,3,6] and Yuwen Qin[1,3,7]

[1]Key Laboratory of Photonic Technology for Integrated Sensing and Communication, Ministry of Education, Institute of Advanced Photonic Technology, School of Information Engineering, Guangdong University of Technology, Guangzhou 510006, China
[2]Department of Electronic and Electrical Engineering, University College London, London WC1E7JE, UK
[3]Guangdong Provincial Key Laboratory of Information Photonics Technology, Institute of Advanced Photonic Technology, School of Information Engineering, Guangdong University of Technology, Guangzhou 510006, China
[4]Department of Electrical and Electronic Engineering, The Hong Kong Polytechnic University, Hong Kong, China
[5]Key Laboratory of Micro-Nano Electronic Devices and Smart Systems of Zhejiang Province, College of Information Science and Electronic Engineering, Zhejiang University, Hangzhou 310027, China
[6]e-mail: yixu@gdut.edu.cn
[7]e-mail: qinyw@gdut.edu.cn
[†]These authors contributed equally to this work.

Received 17 May 2024; revised 11 September 2024; accepted 8 October 2024; posted 8 October 2024 (Doc. ID 530245); published 2 December 2024

Dispersion management in guided wave optics is of vital importance for various applications. Topological photonics opens new horizons for manipulating unidirectional guided waves utilizing edge states. However, the experimental observation of spatiotemporal dynamics for guided waves with on-demand dispersion in topological photonic crystal is an important issue awaiting exploitation. Herein, we experimentally investigate the spatiotemporal properties of topological surface states with on-demand dispersion, where they are supported by a truncated valley photonic crystal with surface modulation. We observe the electromagnetic dynamics of surface states with typical dispersions, where dynamical trapping of an electromagnetic pulse mediated by the unidirectional surface state with flat dispersion and backward beam routing using reversed dispersion properties are achieved in photonic crystal slabs. Both numerical and experimental results substantiate the ultimate dispersion management for topological surface states, which could pave new ways for the manipulation of electromagnetic waves on the surface of photonic devices.

https://doi.org/10.1364/PRJ.530245

1. INTRODUCTION

Surface states are an interesting wave phenomenon that exists in various kinds of wave systems [1], such as Shockley electronic states at terminated semiconductors [2], elastic waves on the surfaces of solids [3], and surface plasmon polaritons [4,5]. They possess distinct physical properties that are absent in bulk media, facilitating numerous fundamental discoveries and important applications leveraged by their unique surface nature, including but not limited to topological physics [6–8], photonic time crystals [9], communications [10,11], three-dimensional waveguiding [12,13], unidirectional propagation [14,15], lasing [16], and sensing [17], just to name a few.

Topological physics provides a new twist in manipulating guided waves at an interface, where unidirectional transmission immune to certain types of defects can be achieved [18,19]. As a result, topological photonic crystals (PhCs), especially PhC slabs supporting topological edge states, have attracted great attention because of their capability in manipulating light at chip scale. To date, several kinds of quantum-Hall-related topological electronic states in condensed matter physics have been extended to photonic systems [20–37], facilitating various on-chip applications [34,38–48]. In particular, dispersion management of topological PhCs can also provide an effective approach to realize precise manipulation of light. The dispersion management of either bulk bands or topological edge states enables new possibilities to realize higher-order topology [49,50], topological lasers [51], topological slow light [32,33,52,53], and topological rainbow trapping [54–56]. However, interfacing two PhCs with opposite topological properties is indispensable to sustain topological edge states, which substantially limits the

on-demand dispersion manipulation of these edge states. Topological surface states provide an effective means to overcome this limitation, which offer more degrees of freedom to modulate the dispersion of surface states [57–60]. Although dispersion management of surface waves is crucial for achieving versatile functionalities [6–9], on-demand manipulation of dispersion properties of the topological surface waves remains a promising but unsolved challenge. More importantly, the observation of spatiotemporal dynamics for these surface waves with on-demand dispersion, which can pinpoint handcrafted dispersion, is also absent, which prevents the advanced manipulation of electromagnetic (EM) surface waves in spatiotemporal dimensions.

In this paper, we theoretically propose and experimentally demonstrate a concept of topological surface states with on-demand dispersion, as shown in Fig. 1(a). The proposed topological surface states, where the electromagnetic field localizes at the interface between the PhC slab with modulated boundary cylinders and the air, are supported by a truncated valley PhC with surface modulation, which provides more degrees of freedom for achieving on-demand dispersion management of the surface states. Both the direction and magnitude of group velocity ($v_g = \mathrm{d}\omega/\mathrm{d}k_x$, where ω is the angular eigenfrequency) of the surface states can be tailored substantially. Microwave experiments for the observation of dynamical spatial trapping of EM surface waves with flat dispersion in the time domain and topological surface waves with opposite group velocities

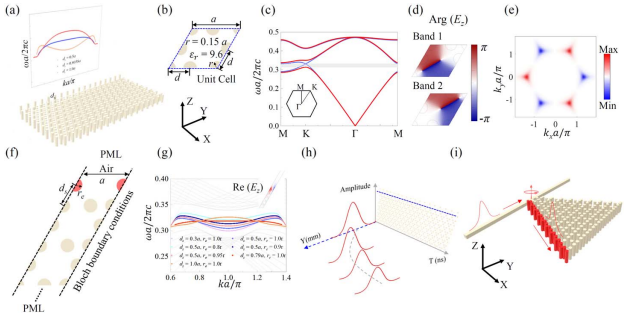

Fig. 1. Topological surface states with on-demand dispersion. (a) Schematic of the topological surface states with on-demand dispersion. The dispersion of the topological surface states can be effectively manipulated by modifying the structural parameter d_s. (b) The unit cell of the 2D kagome PhC supporting topological surface states. The lattice constant is a, and the 2D unit cell is formed by three dielectric cylinders with a radius $r = 0.15a$. The relative permittivity ε_r is 9.6. (c) Band diagrams of kagome PhCs with (blue, $d = 0.5a$) and without (red, $d = 0.56a$) inversion symmetry. The valley gap generated at the K point by breaking the inverse symmetry of the unit cell is indicated by the gray region. (d) Phase distributions of E_z at the K point for the first and second bands. (e) Berry curvature for the first band of the unit cell without inversion symmetry shown in (c). (f) The super cell of the 2D PhC supporting topological surface states. The radius of the boundary cylinder is r_e, and the distance between the boundary cylinder and the PhC is d_s. (g) The eigenmode dispersion of the super cell shown in (f) with different structural parameters, where a typical electric field distribution Re(E_z) of the surface state is also provided in the inset. (h), (i) Schematics for the dynamical spatial trapping of the EM pulse and backward beam routing mediated by topological surface states with on-demand dispersion, respectively.

serve as two typical examples to validate the proposed concept. Our results could bring new insight in designing surface wave based integrated devices with functional applications, such as optical buffer, high-Q cavity, and backward beam routing.

2. RESULTS

A. Physical Properties of the Two-Dimensional PhC

The two-dimensional (2D) PhC is considered first, which will be generalized to a three-dimensional (3D) case, i.e., a PhC slab, in the next section. The 2D unit cell of the kagome PhC with lattice constant a approximately equal to 26.7 mm is shown in Fig. 1(b), which consists of three dielectric cylinders in air with a radius of $r = 0.15a$ and relative permittivity of $\varepsilon_r = 9.6$. The height of the cylinders is infinite in the 2D case. The inversion symmetry of the unit cell can be tuned by adjusting the structural parameter d. The band structures for the transverse magnetic (TM) modes (E_z polarized) of the kagome PhC with ($d = 0.5a$) and without ($d = 0.56a$) inversion symmetry are shown in Fig. 1(c). A Dirac point is formed between the first and second bands at the K/K' point when the inversion symmetry of the unit cell is maintained. Moreover, when the inversion symmetry of the PhC is broken (for example, $d = 0.56a$), the Dirac point will be gapped out, giving rise to a valley gap marked by the gray shadow, as shown in Fig. 1(c). The phase distributions of the eigenmodes (E_z) at the K point for the bands below and above the valley gap are shown in Fig. 1(d), from which one can see that the phase windings of the two bands are opposite, indicating their distinct topological properties. The non-trivial topology in momentum space can be characterized by the Berry curvature,

$$\mathcal{F}(\mathbf{k}) = \nabla_{\mathbf{k}} \times \mathcal{A}_n(\mathbf{k}), \tag{1}$$

where

$$\mathcal{A}_n(\mathbf{k}) = \langle u_{n\mathbf{k}} | i\nabla_{\mathbf{k}} | u_{n\mathbf{k}} \rangle \tag{2}$$

is the Berry connection and $|u_{n\mathbf{k}}\rangle$ is the spatially periodic part of the Bloch function for the nth band. The Berry curvature distribution of the first band below the valley gap is shown in Fig. 1(e), which exhibits opposite signs at the K and K' points, indicating that gapping out the Dirac points can lead to nontrivial valley Chern numbers at K/K' (note that the second band above the valley gap has the opposite feature to the first band and is thus not shown here).

By truncating the non-trivial PhC with a valley gap using boundary cylinders with a radius r_e in the 2D super cell shown in Fig. 1(f), topological surface states with on-demand dispersion can be obtained, where Bloch and perfectly matched layer (PML) boundary conditions used in the simulations are also marked in the figure. Because of the surface state nature, one has more degrees of freedom to manipulate the dispersion properties of the topological surface states by modifying the structural parameters of the boundary cylinders. The radius r_e of the boundary dielectric cylinders and the distance d_s between the boundary cylinders and the bulk PhC are the key parameters to achieve on-demand dispersion of the topological surface states. The calculated eigenmode dispersions for seven typical cases in terms of d_s and r_e indicated in Fig. 1(f) are shown in Fig. 1(g) (see Appendix A). It can be seen that the dispersion of the surface states is changed from concave to

convex by simply tuning d_s. It means that the direction and magnitude of the corresponding v_g for the surface states can be substantially modified, leading to reversed dispersion properties (see Appendix C). Because the dispersion of the surface states experiences continuous shape change, a flat dispersion can be achieved in the intermediate stage, as shown in Fig. 1(g), facilitating the dynamical spatial trapping of an EM pulse, as shown in Fig. 1(h). As can be seen from Fig. 1(g), changing r_e will mainly shift the dispersion of a given shape, indicating the opportunity for achieving on-demand dispersion management at a given frequency (see Appendix D). At the same time, leveraged by the guided modes with reversed group velocities, on-chip backward beam routing could be achieved, which is presented in Fig. 1(i).

B. Physical Properties of the PhC Slab with Finite Height

As can be seen from the above analysis, the dispersion of the topological surface states in this 2D PhC can be manipulated precisely. Guiding by the total internal reflections at boundaries parallel to the X-Y and X-Z planes, we can generalize the topological surface states from 2D to 3D using a PhC slab with finite height. The schematic unit cell of the 3D kagome PhC is shown in the inset of Fig. 2(a), where the radius of the dielectric cylinders and the lattice constant are the same as those of the 2D PhC, whereas the height of the unit cell is $h = 1.3483a$. In order to obtain a topological bandgap similar to the 2D case, the inversion symmetry of the unit cell is broken ($d = 0.6a$). The band structures for the quasi-TM modes of the kagome PhC slab with (blue line) and without (red line) inversion symmetry are shown in Fig. 2(a), where the results are similar to the 2D cases (see Appendix E). This non-trivial unit cell with a topological bandgap is used to design a super cell that is similar to the 2D one, where the eigenmode dispersions of the surface states with different d_s (see Appendix E) are shown in Fig. 2(b) (see Appendix A). The corresponding group indices ($n_g = c/v_g$, where c is the speed of light in vacuum) are also provided in Fig. 2(c). Similar to the 2D case, the dispersion of the topological surface states also experiences the shape change from concave to convex with an increase of d_s, and the group index approaches infinity when $d_s = 0.8038a$. It means that the v_g of this topological surface state is nearly zero. This interesting phenomenon can be used to achieve dynamical light trapping based on topological surface states. It should be noted that the direction of v_g is reversed for the case of $d_s = 1.0a$ and a partial direction of v_g is reversed for the case of $d_s = 0.7a$, which can also be seen from the band structures shown in Fig. 2(b). Additionally, the mapping relationship among v_g, d_s, and r_e is too complex to be retrieved, which is out of the scope of this paper. The data-driven deep learning method could be a solution [61]. Figures 2(d) and 2(e) show the near-field distributions of the electric field [Re(E_z)], Poynting

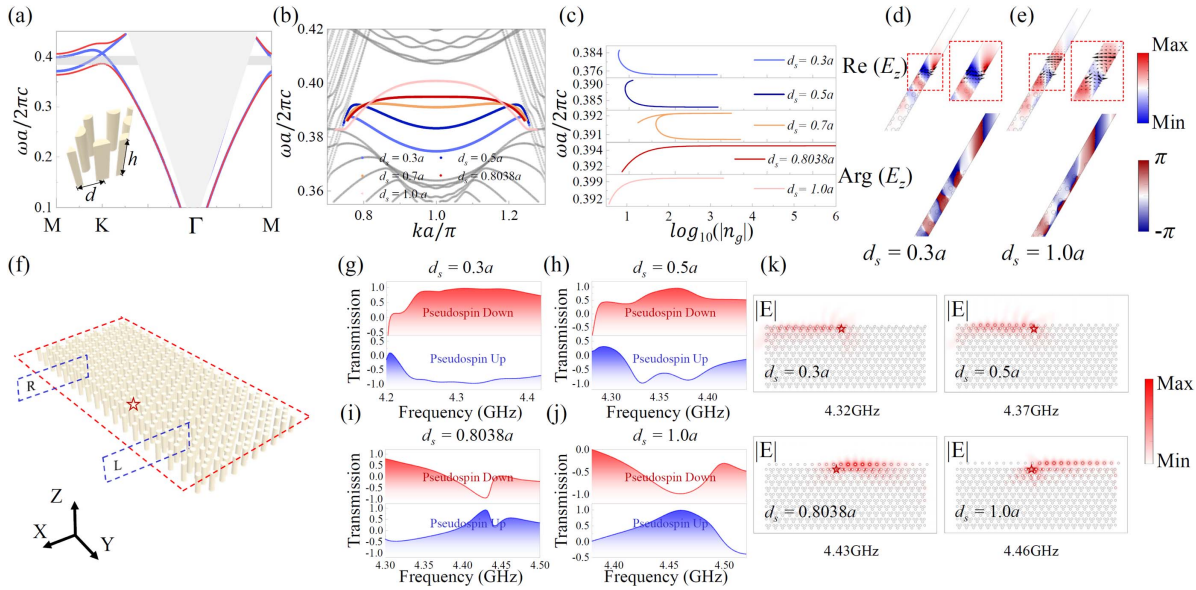

Fig. 2. Eigen- and excitation solutions of topological surface states in a PhC slab. (a) The band diagrams of the kagome PhC with (blue, $d = 0.5a$) and without (red, $d = 0.6a$) inversion symmetry, where the 3D unit cell is shown by the inset. The height of the dielectric cylinders is $h = 1.3483a$. The light and dark gray areas indicate the light cone and the bandgap, respectively. (b) The eigenmode dispersion of the super cell for different structural parameters d_s. (c) The corresponding calculated group indices of the topological surface states for different structural parameters shown in (b). (d), (e) Real parts of E_z, Poynting vectors, and phase distributions of E_z for the cases of $d_s = 0.3a$ and $d_s = 1.0a$, respectively. (f) A finite PhC slab consists of 23 periods along the propagation direction. The red star indicates the location of the CPMD sources, where the energy fluxes P_L and P_R are calculated at two planes indicated by two blue dashed boxes ($1.34a \times 3.75a$) labeled by L and R. Both planes are $3.5a$ away from the boundary of the waveguide along the Y-axis, where parts of them are inside the PhC ($2.2a$ in length) to take the whole surface state into account. The background material is air. (g)–(j) The calculated normalized transmission spectra for different structural parameters d_s, which are obtained by integrating the power in the blue dashed boxes (see Appendix A). The value "1" ("−1") represents the energy flux exclusively to the left (right) side. The red and blue curves represent the transmission spectra under the excitation of pseudospin-down and pseudospin-up CPMD sources, respectively. (k) The corresponding distributions of electric field $|E|$ under the excitation of the same CPMD source (pseudospin-down) shown in (g)–(j), where the red stars indicate the locations of the CPMD sources.

vectors, and its phase distributions Arg(E_z) for the topological surface states when $d_s = 0.3a$ and $d_s = 1.0a$ at $k_x = 1.1\pi/a$, respectively. The corresponding Poynting vectors form a clockwise or anticlockwise rotation around the phase vortex center. Therefore, electromagnetic energy flows from one supercell to its unilateral supercell, forming an effective wave-guiding channel. The near-field distributions for the super cell with other d_s are provided in Appendix E. As can be seen from these figures, a phase vortex center can be clearly identified near the boundary, and the electric field (E_z) is also strongly localized at the truncated surface without any leakage to the air, validating the surface state nature.

To study the propagation properties of the topological surface states with on-demand dispersion, we consider a finite PhC slab (23 periods along the propagation direction) under the excitation of circularly polarized magnetic dipole (CPMD) sources (see Appendix A), as shown in Fig. 2(f). The normalized transmission spectra at different d_s excited by CPMD sources with opposite pseudospin states (see Appendix A) are shown in Figs. 2(g)–2(j), where pseudospin dependent unidirectional propagation of the surface states can be clearly observed. It should be noted that for cases of $d_s = 0.3a$ and $d_s = 1.0a$, the CPMD sources with the same pseudospin state are placed at the same Y position in the waveguide, but their transmission spectra show completely opposite characteristics because of the reversed dispersion properties controlled by d_s. The near-field distributions of the electric field $|E|$ for reversed dispersion properties under the excitation of the pseudospin-down CPMD source are shown in Fig. 2(k), which can intuitively validate the pseudospin-dependent unidirectional transmission characteristic (see Appendix F) and indicate the topological properties of the proposed surface states. In particular, for the case of ultra-flat dispersion ($d_s = 0.8038a$) with nearly zero v_g, the electric field $|E|$ is mainly localized close to the CPMD source, and the dynamical EM wave trapping in the surface waveguide will be demonstrated in the following.

C. Experimental Demonstrations

Microwave experiments are performed to validate the theoretical results, where the experimental setup is shown in Fig. 3(a). A finite topological PhC slab composed of 23 periods along the Y direction is fabricated using alumina ceramic cylinders ($\varepsilon_r = 9.6$, $\tan\delta \approx 4\times10^{-4}$, $r = 4$ mm, and $h = 36$ mm). The boundary cylinders ($r_e = r$, $h = 36$ mm) are introduced at the surface. Because a CPMD source at the considered frequency range is difficult to implement, a magnetic dipole is used to excite the topological surface states in the microwave experiment. A home-made loop antenna is placed inside the finite PhC waveguide, which is presented in the inset of Fig. 3(a) (see Appendix B), where it mimics a magnetic dipole with a dipole moment along the X direction. The normalized spectra $|S_{21}|$ of an electric monopole antenna at the blue star marked in Fig. 3(a) indicate the transmission characteristics of surface states in the topological PhC slab, where different cases of d_s are shown in Figs. 3(b)–3(e) (see Appendix B). The corresponding simulation results calculated by the 3D finite difference time domain (FDTD) method are also provided (see Appendix F). As can be seen from these figures, good agreement between the simulation and experimental results can

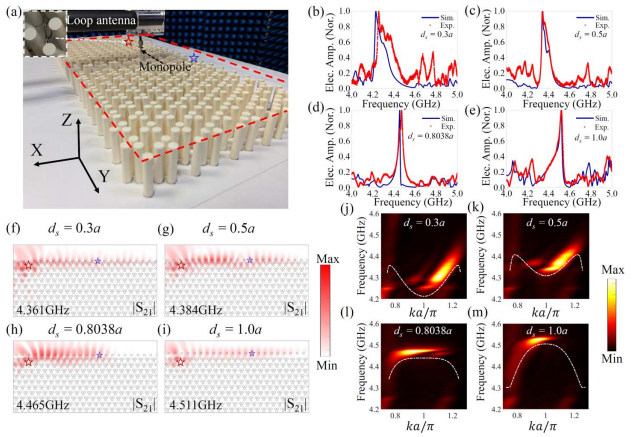

Fig. 3. Steady results of microwave experiments. (a) The experimental setup and fabricated dielectric PhC slab to demonstrate the topological surface states with on-demand dispersion. (b)–(e) Experimentally acquired $|S_{21}|$ (red points) and calculated normalized electric field amplitude $|E_z|$ (blue solid lines) for different structural parameters d_s acquired at the blue star marked in (a) under the excitation of a loop antenna. (f)–(i) The distributions of $|S_{21}|$ for different d_s measured by a monopole antenna at the red dashed box outlined in (a). (j)–(m) Experimentally retrieved band structures calculated by the Fourier transform of the steady states and their corresponding simulation results (white dotted line).

be achieved, which confirms that the proposed topological surface states can be excited effectively by using the loop antenna. Furthermore, the distributions of $|S_{21}|$ measured at the area marked by the red dashed rectangle in Fig. 3(a) for different d_s are provided in Figs. 3(f)–3(i). As can be seen from these experimental results, the EM fields are mainly localized at the surface of the PhC waveguide. Furthermore, the electric field shown in Fig. 3(h) is mainly trapped at the location close to the source, which agrees well with the simulation results shown in Fig. 2(k). Moreover, in order to verify the reversed dispersion properties for the cases of $d_s = 0.3a$ and $d_s = 1.0a$ in experiment, Fourier transform is used to analyze the near-field distribution acquired in experiment, where the corresponding retrieved band structures are shown in Figs. 3(j)–3(m). The corresponding simulation results of eigenmode dispersion (white dashed lines) are also provided, where they qualitatively agree with each other except for small frequency shift caused by the permittivity uncertainty of the cylinders. By increasing d_s, the shape of the dispersion changes continuously, from a concave type to a flat type and to a convex type at last, enabling the realization of on-demand dispersion management for topological surface states. The flattest dispersion is obtained at $d_s = 0.8038a$, which can facilitate the experimental observation of dynamical spatial trapping of EM waves in the time domain.

Then we consider the propagation dynamics of the topological surface states with on-demand dispersion. The simulated spatiotemporal results are calculated by using 3D FDTD method (see Appendix A), where they are presented in the right column of Figs. 4(a)–4(c). In simulation, the central frequencies of the time domain Gaussian pulse are set to 4.361 GHz, 4.465 GHz, and 4.511 GHz for three different d_s, while the

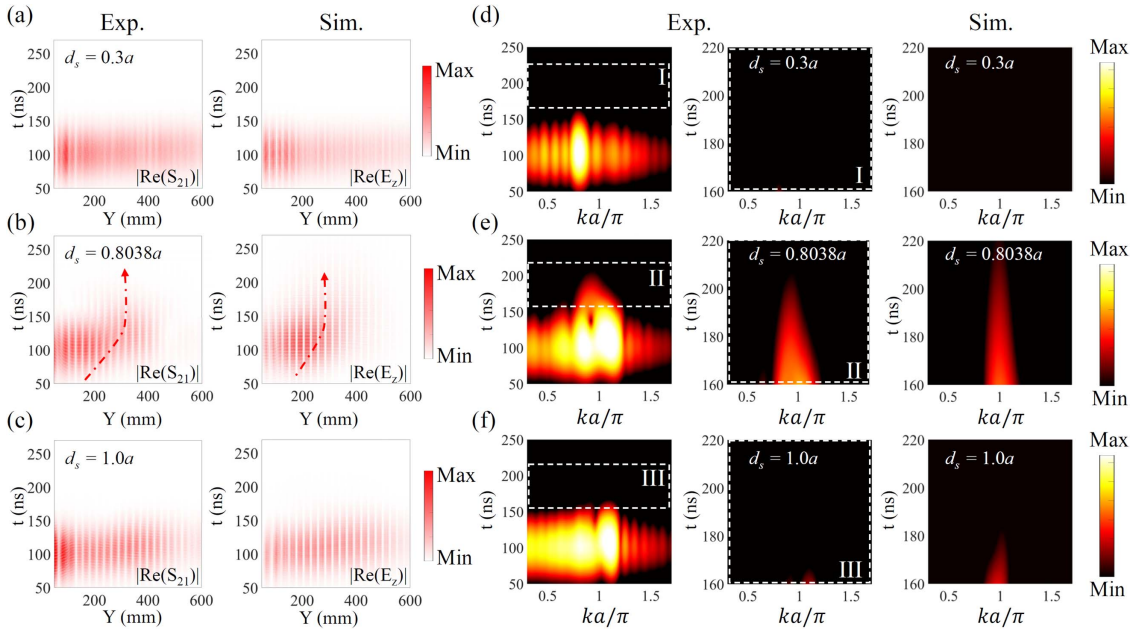

Fig. 4. Spatiotemporal results of microwave experiments. (a)–(c) Evolutions of experimentally retrieved $|\mathrm{Re}(S_{21})|$ in spatial and time domains, which are acquired along the blue line (Fig. 13 in Appendix G), and the corresponding simulation results are also provided. The red arrows marked in (b) indicate the dynamical positions of the Gaussian pulse. (d)–(f) Fourier transform of experimental results at every moment. The zoom-in views for I, II, and III marked by the white dashed boxes are provided. The simulation results are also provided.

width and offset of the Gaussian pulses are set to 40 ns and 100 ns, respectively. As can be seen from Fig. 4(b), the EM pulse is trapped at the position of $Y \approx 11.2a$ for the case of $d_s = 0.8038a$, while for other cases ($d_s = 0.3a$ and $d_s = 1.0a$) shown in Figs. 4(a) and 4(c), the EM pulses can transmit through the PhC along the Y direction. To verify the theoretical results, inverse Fourier transform of the experimentally acquired results in frequency domain is leveraged to validate the dynamical spatial trapping of EM waves mediated by the topological surface states (see Appendix G). The retrieved results of spatiotemporal dynamics in experiment are provided in the left columns of Figs. 4(a)–4(c), whose central frequency, width, and offset of the Gaussian pulses are the same as those used in the simulation. It can be seen that the experimental results agree reasonably well with the simulation ones. For the case with the smallest v_g [$d_s = 0.8038a$ shown in Fig. 4(b)], the electric field is trapped at the center of the waveguide rather than propagating along the waveguide. Meanwhile, the trapping position of the electric field in the waveguide can be effectively manipulated (see Appendix G). This interesting phenomenon may further facilitate the rainbow trapping based on topological surface states [54–56]. Both the observations of different dispersion relationships shown in Figs. 3(j)–3(m) and spatiotemporal dynamics with distinct transmission properties shown in Figs. 4(a)–4(c) consolidate the possibility of flexible dispersion manipulation for topological surface states [62]. We further analyze the time dependent evolutions of surface states in momentum space, where the experimental and simulation results are shown in Figs. 4(d)–4(f). There is a long-life trapping mode for the case of $d_s = 0.8038a$ with the smallest v_g, where this mode exists in the range of 160 ns $< t <$ 220 ns with an almost constant wave number. The lifetime of topological surface states in simulation is longer than the experimental one, which is because of the material losses in the experiment. It also should be noted that this long-life mode still decays because of the finite size effect and material absorption of the PhC slab. Meanwhile, there exists no EM wave for the cases of $d_s = 0.3a$ and $d_s = 1.0a$ that possess higher v_g in this range. This interesting phenomenon indicates that the topological surface states with on-demand dispersion can achieve nearly zero v_g, enabling the observation of dynamical spatial trapping of EM waves in the time domain.

To further provide an intuitive picture, $|S_{21}|$ proportional to the electric field for three different d_s at typical moments are presented in Figs. 5(a)–5(c). The full videos are available in

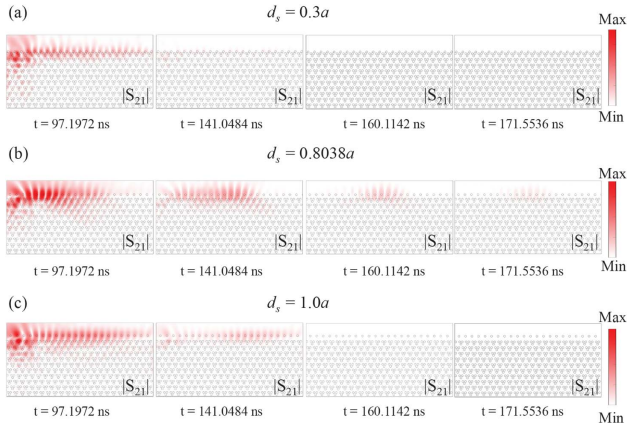

Fig. 5. Snapshots of spatiotemporal results in experiment. (a)–(c) The near-field distributions of $|S_{21}|$ for different d_s at four typical moments.

Visualization 4, Visualization 7, and Visualization 8 (MP4). For the topological surface state with the largest v_g shown in Fig. 5(a), it passes through the waveguide rapidly. With the increase of d_s (see Appendix G), the topological surface state still exists in the waveguide at $t = 141.0484$ ns, which indicates that the v_g of topological surface states is significantly reduced. The case of a flat dispersion ($d_s = 0.8038a$) with the smallest v_g is shown in Fig. 5(b), from which one can see that the topological surface state is effectively trapped at a certain position of the waveguide. Further increasing d_s to $1.0a$, the dispersion property of the surface states reverses, and the corresponding v_g increases, where it can also pass through the waveguide rapidly. According to the time domain data of the experiment, the corresponding v_g for $d_s = 0.3a$, $d_s = 0.5a$, and $d_s = 1.0a$ is $0.16c$, $0.08c$, and $0.13c$, respectively. These results agree well with the experimental results shown in Figs. 3(j), 3(k), and 3(m). It should be noted that the v_g associated with the topological surface state at $d_s = 0.8038a$ is difficult to quantitatively evaluate due to the spatial trapping of the EM wave. However, the corresponding v_g can be approximately evaluated according to the retrieved band structure shown in Fig. 3(l), which is about $0.001c$. This v_g is smaller than the one ($>10^{-6}c$) calculated by eigenmodes because of the finite size effect.

In order to further demonstrate the potential application of the topological surface states with on-demand dispersion, we design a triangular PhC waveguide structure for achieving beam routing, which is presented in Fig. 6(a) (see Appendix H). A dielectric waveguide with a square cross section (side length is 17.6 mm) and a dielectric resonator with a radius of 8 mm as well as a height of 11 mm are used to mimic point sources with different pseudo-spin states [34]. By modifying the input direction of the waveguide, the pseudospin states in the dielectric resonator can be changed effectively to realize unidirectional transmission. The normalized electric field amplitudes as a function of the frequency for $d_s = 0.3a$ and $d_s = 1.0a$ at the blue and red stars in the transmission direction are shown in Figs. 6(b) and 6(c), respectively (see Appendix B). The simulation results qualitatively agree with the experimental results, where the frequency shift between the simulation and experimental results may come from the difference of permittivity or size used between experiments and simulations. The corresponding near-field distributions $|S_{21}|$ of the steady states are provided in Figs. 6(d) and 6(e), and the dynamical results are provided in Figs. 6(f) and 6(g). The unidirectional transmission with very small backward scattering in both steady and dynamical results further consolidates that the proposed surface states possess topological properties. Meanwhile, these experimental results can also indicate that reversed dispersion properties can be achieved by modifying the structural parameter d_s. Red arrows and blue triangles indicate the propagation directions of the EM pulse and the location of the PhC slab structure, respectively. It can be seen that reversed dispersion properties can be used to route the EM pulse along different directions, where negative propagation direction with respect to the input one can also be achieved as shown in Figs. 6(d) and 6(f). As demonstrated by all the simulation and experimental results, the proposed topological surface states with on-demand dispersion provide promising opportunities to precisely tailor the magnitude and direction of v_g on the surface of photonic devices. Furthermore, our proposed PhC slab can effectively reduce the size of topological optical devices, facilitating compact optical integration of topological photonic devices.

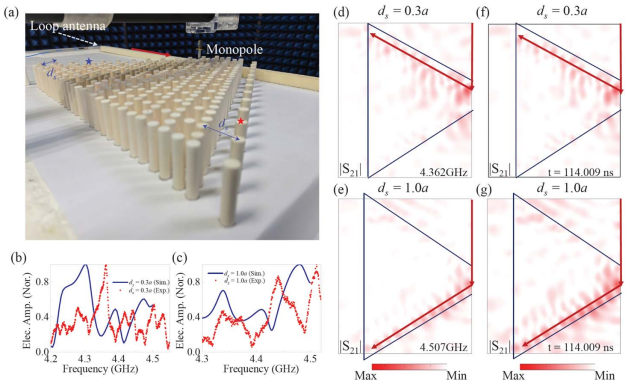

Fig. 6. Experimental results of backward beam routing. (a) The experimental setup and fabricated dielectric PhC slab to demonstrate the beam routing effect. (b), (c) Experimentally acquired $|S_{21}|$ (red points) and simulated electric field amplitude $|E_z|$ (blue solid lines) for different structural parameters d_s obtained at the positions marked by the blue and red stars in (a), respectively, where the excitation of the loop antenna is placed on the dielectric waveguide. (d), (e) The acquired distribution of $|S_{21}|$ for $d_s = 0.3a$ and $d_s = 1.0a$ measured by a monopole antenna. Red arrows and blue areas indicate the direction of transmission and the location of the PhC slab, respectively. (f), (g) The typical near-field distributions of $|S_{21}|$ at a specified moment ($t = 114.009$ ns). The central frequencies of the reconstructed pulses are set to 4.362 GHz and 4.507 GHz, respectively. And the corresponding pulse width and offset are set to 40 ns and 100 ns, respectively.

3. DISCUSSION AND CONCLUSION

In summary, we theoretically propose and experimentally demonstrate a concept of topological surface states with on-demand dispersion. The dispersion properties of the surface guided modes can be feasibly tailored by changing the structural parameters of the boundary cylinders. The ultimate management of dispersion for the topological surface states enables the direct experimental observation of dynamical EM pulse trapping. Our experimental results validate the existence of topological surface states, and their EM dynamics further confirms the on-demand dispersion management. The unprecedented dispersion management of topological surface wave states might provide a paradigm shift for dispersion engineering in topological PhCs, which not only enables the on-demand manipulation of topological surface guided waves, but also effectively reduces the size of topological waveguides compared with conventional PhC waveguides based on topological edge states between two different PhCs. It is anticipated that our findings could pave new ways for the ultimate management of dispersion for the topological surface waves and shed new light on designing topological microcavities with higher Q factor, surface state based rainbow trapping, and functional optical integration of topological PhC devices.

APPENDIX A: NUMERICAL METHOD

For the eigen-solutions, the eigenmode dispersions of the bulk PhC and the surface states are calculated by the finite-element method (FEM). In order to calculate the dispersion of bulk PhC or surface states of the 2D and 3D cases, Bloch boundary conditions and PMLs are applied at the boundaries of the unit or super cell shown in Figs. 1(b) and 1(f), while PMLs are also used in the $\pm Z$ directions for the 3D unit cell and super cell. For the excitation solutions, the unidirectional topological surface states excited by the CPMD sources shown in Fig. 2(f) are also calculated by using FEM. CPMD sources are composed of two orthogonal magnetic dipole emitters with dipole moments in the X and $Y(-Y)$ directions to mimic the local pseudospin-down (pseudospin-up) source. The energy flux P_L (P_R) as a function of excitation frequency in the 2D PhC case is calculated at the dashed line L (R) marked in Fig. 7(a) of Appendix C using a pseudospin-down (pseudospin-up) source, and the corresponding results for 3D cases are calculated in the blue dashed box L (R) marked in Fig. 2(f). Based on these results, the normalized transmission spectra (T_N) can be defined in Eq. (A1),

$$T_N = \frac{P_L - P_R}{P_L + P_R}. \tag{A1}$$

The broadband transmission responses and time domain simulation results of the surface states considered in experiment are calculated by using FDTD method, which are all excited by a magnetic dipole source. PMLs are used in the $\pm X$, $\pm Y$, and $\pm Z$ directions.

APPENDIX B: MICROWAVE EXPERIMENT

The experimental setup for performing the near-field measurement of the S parameters proportional to certain components of the electromagnetic fields is shown in Fig. 3(a). A home-made loop antenna mimicking a magnetic dipole with the dipole moment along the X direction is connected to a vector network analyzer (VNA, R & S ZNA67), which is used to generate a dipole like radiative EM wave (4 to 5 GHz). In order to map out the corresponding electric field ($|E_z|$) distribution on the surface of the PhC slab, the electric monopole antenna is used, whose $|S_{21}|$ is acquired at the rectangle region marked in Fig. 3(a). The antenna is mounted on a scanning platform (LINBOU, NFS03 Floor Version) connected to the VNA. As a result, $|S_{21}|$ proportional to the electric field component as a function of frequency and position can be obtained. The PhC slab is placed on a foam substrate ($\varepsilon_r \approx 1$), whose permittivity is similar to air, and the substrate effect can be neglected. Microwave absorbers are used to minimize the impact of echo signals. Based on the experimental data $S_{21}(x, y, \omega)$ obtained from the electric monopole antenna, the propagation dynamics of the topological surface states can be retrieved by using the inverse Fourier transform [63]. A time domain pulse produced by a magnetic dipole source is used to excite the topological surface states, whose corresponding spectrum can be represented by $G(\omega - \omega_0)$, where ω_0 is the central frequency. The measured data $S_{21}(x, y, \omega)$ or simulated steady state solutions in the frequency domain are filtered by the spectrum of a targeted retrieved EM pulse,

$$S(x, y, \omega) = S_{21}(x, y, \omega) G(\omega - \omega_0), \tag{B1}$$

and then the corresponding time domain results can be acquired by applying the inverse Fourier transform to Eq. (B1),

$$S_{21}(x, y, t) = \frac{1}{2\pi} \int S(x, y, \omega) e^{i\omega t} \mathrm{d}\omega. \tag{B2}$$

In order to verify the accuracy of the experimental data, 3D FDTD results are used to validate the retrieved EM wave propagation dynamics of the topological surface states.

APPENDIX C: EXCITATION OF TOPOLOGICAL SURFACE STATES IN THE 2D PHC STRUCTURE

The normalized transmission spectra for the reversed cases of concave ($d_s = 0.3a$) and convex ($d_s = 1.0a$) dispersion excited by CPMD sources with opposite pseudospin states (see Appendix A) are shown in Figs. 7(b) and 7(c), where pseudospin dependent unidirectional propagation of the topological surface states can be clearly observed. It should be pointed out that the same CPMD source is placed at the same position in the waveguide, which is marked by the red star shown in Fig. 7(a), but their transmission spectra show completely opposite characteristics because of the reversed dispersion properties manipulated by d_s. The near-field distributions of the electric field $|E|$ for reversed dispersion properties under the excitation of the pseudospin-down and pseudospin-up CPMD sources are shown in Figs. 7(d) and 7(e), which can further validate the pseudospin dependent unidirectional transmission characteristic mediated by the reversed dispersion properties.

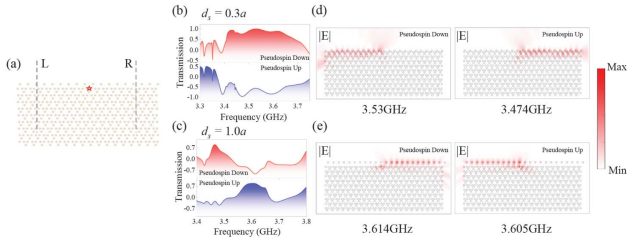

Fig. 7. Excitation solutions of topological surface states in the 2D PhC structure. (a) Schematic of the 2D PhC structure for topological surface states. The location of CPMD sources is marked by the red star. (b), (c) The calculated normalized transmission spectra for topological surface states with different structural parameters d_s, which can be obtained by integrating the power along the gray dashed lines (L and R) marked in (a) (see Appendix A). The red and blue curves represent the transmission spectra under the excitation of pseudospin-down and pseudospin-up CPMD sources, respectively. (d), (e) The corresponding distributions of electric field $|E|$ under the excitation of CPMD sources with opposite pseudospin states.

APPENDIX D: TOPOLOGICAL SURFACE STATES OF 2D PHC STRUCTURES WITH DIFFERENT STRUCTURAL PARAMETERS

Because of the nature of surface states, one has more degrees of freedom to manipulate the dispersion properties of the topological surface states by modifying the geometry parameters at the boundary of the super cell. In order to further validate that on-demand management of the dispersion of topological surface states can be realized by the proposed PhC structure, we calculate the eigenmode dispersion of the topological surface states with various structural parameters, as shown in Figs. 8(a) and 8(c). As can be seen from these figures, the dispersion of the surface states is changed from concave to convex by simply changing d_s, which indicates that the direction and magnitude of the corresponding group velocity (v_g) for the surface states can be substantially modified. Furthermore, by changing r_e, the normalized frequencies of dispersion of the topological surface states can also be modulated effectively while keeping the v_g almost unchanged. Figure 8(b) provides the near-field distributions of electric field [Re(E_z)] and its phase distributions [Arg(E_z)] for the surface states when $d_s = 0.3a$, $d_s = 0.71a$, and $d_s = 1.0a$ at $k_x = 1.1\pi/a$, respectively. At the same time, the near-field and phase distributions of E_z for different r_e are also provided in Fig. 8(d) when $d_s = 0.5a$. As can be seen from these figures, a phase vortex center can be clearly identified near the boundary, and the electric field (E_z) is also strongly localized at the truncated surface without any leakage to the air, validating the surface state nature. As a result, the shape of dispersion for topological surface states can be manipulated effectively by changing d_s while the normalized frequencies of topological surface states can also be controlled by changing r_e, enabling the on-demand dispersion of topological surface states.

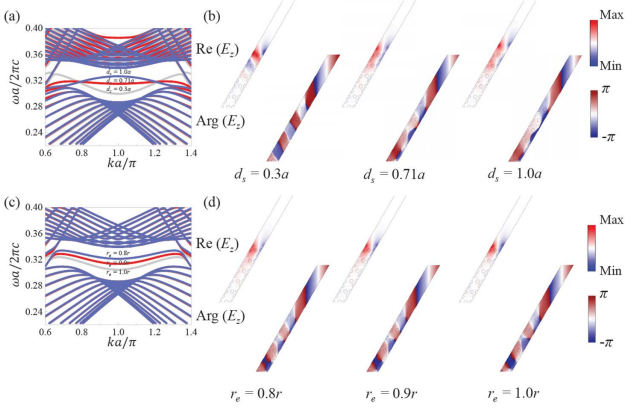

Fig. 8. Eigen-solutions of topological surface states in a 2D PhC structure. (a) The eigenmode dispersion of the super cell shown in Fig. 1(f) with different structural parameters d_s. (b) The corresponding distributions of Re(E_z) and Arg(E_z) for the topological surface states at $k_x = 1.1\pi/a$ shown in (a). (c) The eigenmode dispersion of the super cell shown in Fig. 1(f) with different structural parameters r_e. Here, $d_s = 0.5a$ (a is the lattice constant). (d) The corresponding distributions of Re(E_z) and Arg(E_z) for the topological surface states at $k_x = 1.1\pi/a$ shown in (c).

APPENDIX E: TOPOLOGICAL SURFACE STATES OF PHC SLABS WITH DIFFERENT STRUCTURAL PARAMETERS

Guided by the total internal reflections at the X–Y and Y–Z planes, one can generalize the 2D topological surface state to its 3D counterpart using a PhC slab with a finite height. The schematic unit cell of the 3D kagome PhC is shown in Fig. 9(a), where the lattice constant and radius of the dielectric cylinders are the same as those of the 2D PhC and the height of the unit cell is $h = 1.3483a$. In order to obtain a topological bandgap similar to the 2D structure, the inversion symmetry of the unit cell is broken by $d = 0.6a$. The band structures for the quasi-TM modes of the kagome PhC slab with (blue line) and without (red line) inversion symmetry are shown in Fig. 9(b), where the results are similar to the 2D cases. The light and dark gray areas represent the light cone and the bandgap, respectively. The distributions of Re(E_z) and Arg(E_z) for the structure with inversion symmetry at the K point are shown in Figs. 9(c) and 9(d), while the results of structure without inversion symmetry are provided in Figs. 9(e) and 9(f). As can be seen from these figures, when the inversion symmetry of the unit cell is broken, the phase windings of the K valley states appear in the unit cell of the valley PhC, which indicates that gapping out the Dirac points leads to non-trivial PhC with a topological valley gap. This non-trivial unit cell is used to construct a super cell that is similar to the 2D super cell. The schematic of the 3D super cell is shown in Fig. 9(g). The corresponding distributions of Re(E_z) and Arg(E_z) for the surface states when $d_s = 0.5a$, $d_s = 0.7a$, and $d_s = 1.0a$ at $k_x = 1.1\pi/a$ are also provided. As can be seen from these figures, a phase vortex center can be clearly identified within the boundary sites, and the electric field (E_z) is also strongly localized around the truncated boundary without any leakage to the air, similar to the 2D case.

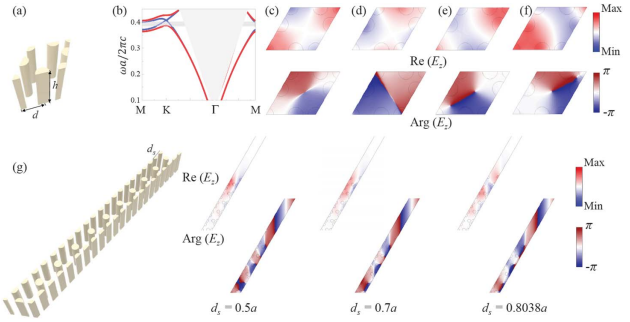

Fig. 9. Topological surface states in a PhC slab with finite height. (a) The 3D unit cell of the kagome PhC supporting topological surface states. The lattice constant is a, and the 3D unit cell is formed by dielectric cylinders with a radius $r = 0.15a$ and a height $h = 1.3483a$. The relative permittivity ε_r is 9.6. (b) The band diagrams of the kagome PhC with (blue, $d = 0.5a$) and without (red, $d = 0.6a$) inversion symmetry. The light and dark gray areas indicate the light cone and the bandgap, respectively. (c), (d) Distributions of Re(E_z) and Arg (E_z) of the gapless PhC at the K point for the first and second bands. (e), (f) Distributions of Re(E_z) and Arg(E_z) of the non-trivial PhC with a valley gap at the K point for the first and second bands. (g) The 3D super cell of the PhC slab supporting topological surface states. The corresponding distributions of Re(E_z) and Arg(E_z) at $k_x = 1.1\pi/a$ for different structural parameters d_s are also provided.

APPENDIX F: EXCITATION OF TOPOLOGICAL SURFACE STATES IN THE PHC SLAB

The near-field distributions of the electric field $|E|$ for different structural parameters d_s under the excitation of the pseudospin-up CPMD source are shown in Figs. 10(a)–10(d), where pseudospin dependent unidirectional propagation of the topological surface states can be clearly observed. It should be pointed out that for the cases of $d_s = 0.3a$ and $d_s = 1.0a$, the same CPMD source is placed at the same Y position in the waveguide marked by the red star shown in Fig. 2(f), but their transmission spectra show completely opposite characteristics because of the reversed dispersion properties manipulated by d_s, as shown in Fig. 2(b). In particular, for the case of ultra-flat dispersion ($d_s = 0.8038a$) with nearly zero v_g shown in Fig. 10(c), the electric field $|E|$ is mainly localized close to the CPMD source, which indicates that the EM wave is dynamically trapped in the middle of the waveguide. Because a CPMD source in the considered frequency range is difficult to be fabricated, a magnetic dipole with a dipole moment along the X direction is used to excite topological surface states in the microwave experiments. As a result, we also calculate the near-field distributions of $|E_z|$ at specified frequencies for the finite topological PhC slab under the excitation of a magnetic dipole source, which are provided in Figs. 11(a)–11(d) (see Appendix A). As can be seen from these figures, the EM fields are mainly localized at the surface of the PhC waveguide without any leakage to the air. Furthermore, the electric field shown in Fig. 11(c) is mainly trapped at the location close to the source, which agrees well with the cases using CPMD sources shown in Fig. 2(k).

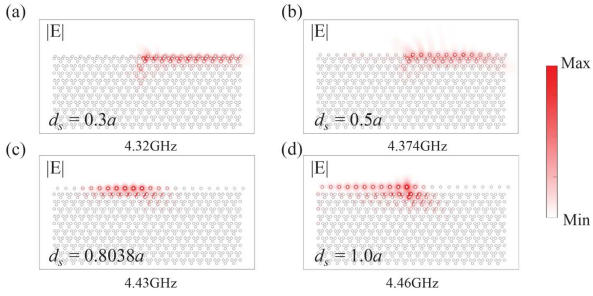

Fig. 10. Excitation solutions of topological surface states in the PhC slab. (a)–(d) The distributions of electric field $|E|$ under the excitation of the same CPMD source (pseudospin-up) for the cases of $d_s = 0.3a$, $d_s = 0.5a$, $d_s = 0.8038a$, and $d_s = 1.0a$.

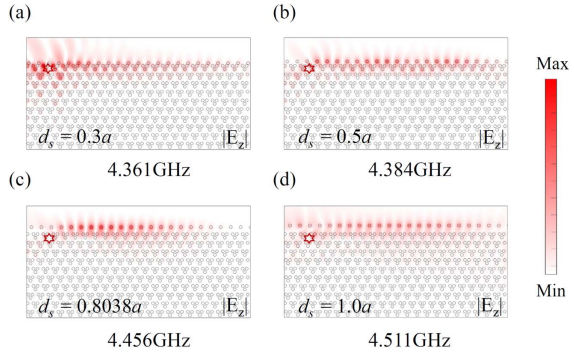

Fig. 11. Topological surface states under the excitation of the magnetic dipole source. (a)–(d) The near-field distributions of electric field amplitude ($|E_z|$) for the cases of $d_s = 0.3a$, $d_s = 0.5a$, $d_s = 0.8038a$, and $d_s = 1.0a$. The red star represents the location of the magnetic dipole source.

APPENDIX G: PROPAGATION DYNAMICS OF THE TOPOLOGICAL SURFACE STATES IN THE PHC SLAB

We further consider the propagation dynamics of the topological surface states with on-demand dispersion. The inverse Fourier transform is used to postprocess the frequency domain data to retrieve the time dependent near-field distribution of topological surface states (see Appendix B). A fixed carrier with Gaussian envelope generated by a magnetic dipole in the time domain,

$$E_t = \sin(-w_0(t - t_0))e^{-((t-t_0)/2\sigma)^2}, \tag{G1}$$

where ω_0 is the central frequency, t_0 is the offset, and $\sigma = \mathrm{PW}/(2\sqrt{\log(2)})$ (PW is the pulse width) is used to excite the topological surface states in the PhC slab. The frequency domain data are the S parameters acquired by the VNA (see Appendix B) or the simulation data calculated by using FDTD method (see Appendix A). Then, the inverse Fourier transform of the frequency domain data is performed to obtain the evolution dynamics of the topological surface states in the time domain (see Appendix B).

To benchmark the retrieved results, we use the frequency domain data extracted from the 3D FDTD simulations to retrieve the dynamics of the topological surface states first. The frequency dependent distributions of electric field E_z in the frequency range of 4–5 GHz at the red dashed box shown in Fig. 12(a) are calculated. Then, the dynamical results in time

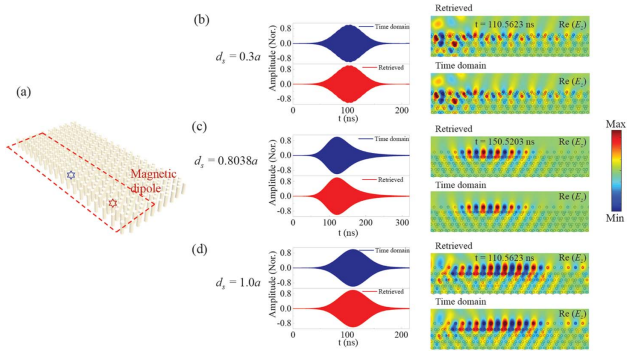

Fig. 12. Benchmarks of the retrieved propagation dynamics using simulated data in the frequency domain. (a) A finite PhC slab supporting topological surface states. The location of the magnetic dipole is marked by the red star. The distributions of Re(E_z) in the frequency and time domains are extracted by the 3D FDTD method at the red dashed box. (b)–(d) Retrieved time dependent Re(E_z) using the frequency domain data obtained by the 3D FDTD method and the direct output results of the 3D FDTD method at the blue star marked in (a). The retrieved near-field distributions [Re(E_z)] at the red dashed box and the direct output results of the 3D FDTD method at typical moments are also provided. The central frequencies of the Gaussian pulse are set to 4.361 GHz, 4.465 GHz, and 4.511 GHz for the cases of $d_s = 0.3a$, $d_s = 0.8038a$, and $d_s = 1.0a$, respectively, while the width and offset of all pulses are 40 ns and 100 ns, respectively.

domain of the topological surface states are retrieved by using the inverse Fourier transform. The retrieved time dependent $\mathrm{Re}(E_z)$ using the simulated frequency domain data at the blue star marked in Fig. 12(a) and the distributions of $|\mathrm{Re}(E_z)|$ at typical moments in time are provided in Figs. 12(b)–12(d) (full details can be found in Visualization 1, Visualization 2, and Visualization 3, MP4). These results are compared with the ones directly outputted from the 3D FDTD simulations. The retrieved results are consistent with the numerical simulations in the time domain. Based on these results, we can confirm that the propagation dynamics of the topological surface states in our experiments can be effectively analyzed by utilizing the retrieval strategy. We further study the propagation dynamics of the topological surface states with on-demand dispersion in a finite PhC slab shown in Fig. 13(a) via microwave experiment. The dynamical results in the time domain are also calculated by using the 3D FDTD method (see Appendix A), where they are presented in Figs. 13(b) and 13(c). In simulation, the central frequencies of the Gaussian pulse are 4.384 GHz and 4.427 GHz for the cases of $d_s = 0.5a$ and $d_s = 0.7a$, respectively, while the width and offset of the Gaussian pulses are 40 ns and 100 ns, respectively. As can be seen from these figures, the EM pulse is trapped at the position of $Y \approx 15a$ for the case of $d_s = 0.7a$. And for the case of $d_s = 0.5a$, the EM pulses can transmit through the PhC slab along the Y direction rapidly. To verify the theoretical results, we retrieve the propagation dynamics using the acquired experimental results in frequency domain to validate the dynamical trapping of the EM pulse mediated by topological surface states with a flat dispersion. The corresponding retrieved pulse propagation dynamics are also provided in Figs. 13(b) and 13(c), whose center frequencies, widths, and offsets of the Gaussian pulses are the same as those in the simulation. It can be seen that the experimental results agree well with the simulated ones (see Appendix B). For the case with a smaller v_g ($d_s = 0.7a$), the electric field is trapped at the waveguide rather than propagating through the waveguide. The difference between experimental and simulation results may be due to the difference in

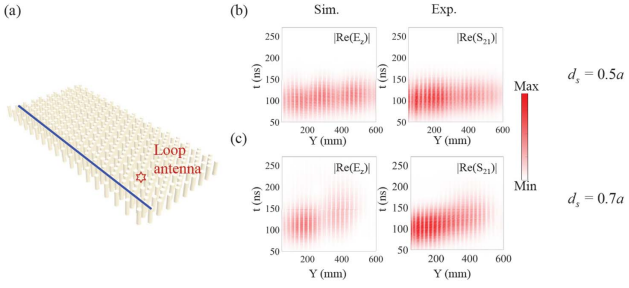

Fig. 13. Propagation dynamics of topological surface states. (a) Schematic of the finite PhC slab supporting topological surface states. The location of the magnetic dipole is marked by the red star. (b), (c) Evolutions of experimentally retrieved $\mathrm{Re}(S_{21})$ in time domain for the cases of $d_s = 0.5a$ and $d_s = 0.7a$, which are both acquired along the blue line shown in (a). The corresponding 3D FDTD results are also provided. The central frequencies of the Gaussian pulses are set to 4.384 GHz and 4.427 GHz for the cases of $d_s = 0.5a$ and $d_s = 0.7a$, respectively, while the width and offset of the two pulses are 40 ns and 100 ns, respectively.

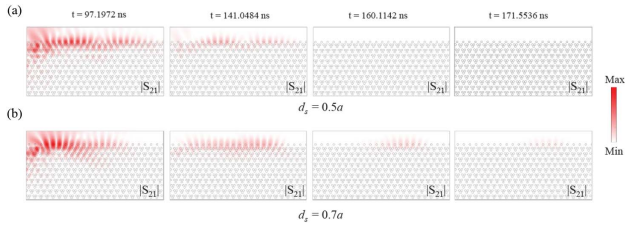

Fig. 14. Snapshots of time domain experimental results. (a), (b) The near-field distribution of $|S_{21}|$ for the cases of different d_s at four typical moments.

material properties used in the simulation and experiment. To provide an intuitive picture, the retrieved $|S_{21}|$ proportional to the electric field for two cases of d_s at various specified moments in time are presented in Figs. 14(a) and 14(b) (full details can be found in the Visualization 5 and Visualization 6, MP4). For the case of $d_s = 0.5a$, the topological surface state still exists in the waveguide at $t = 141.0484$ ns, which indicates that the v_g of topological surface states is lower than the case of $d_s = 0.3a$. Moreover, with the increase of d_s to $0.7a$ with a higher v_g, the EM wave is trapped by the topological surface states rather than transmitting to the end of the waveguide. Interestingly, compared with the case of $d_s = 0.8038a$, the EM wave is trapped closer to the end of the waveguide because its v_g is larger than the case of $d_s = 0.8038a$. These results agree well with the results of group indices shown in Fig. 2(c).

APPENDIX H: THE PHC SLAB STRUCTURE FOR BEAM ROUTING

The top view of the beam routing structure is shown in Fig. 6(a). The overall structure for the beam routing is composed of a topological surface waveguide at the surface of a kagome PhC with a triangle shape, a dielectric resonator, and a dielectric waveguide with a square cross section (the side length is 17.6 mm). The radius and height of the dielectric resonator are 8 mm and 11 mm, respectively, which is used to mimic

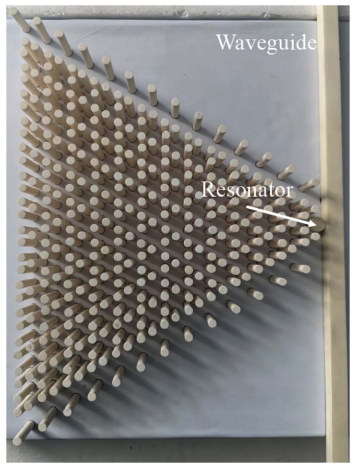

Fig. 15. The PhC slab structure for beam routing. The top view of the PhC structure and the straight coupling waveguide shown in Fig. 6.

point sources with different pseudo-spin states. When the EM waves produced by a magnetic dipole are coupled from above (below) to the waveguide shown in Fig. 15, it will generate an anticlockwise/clockwise phase vortex at the dielectric resonator [34]. Therefore, the direction of the unidirectional transmission of the topological surface states can be manipulated, where a beam router can be achieved.

Funding. National Natural Science Foundation of China (62222505, 62335005); Guangdong Introducing Innovative, Entrepreneurial Teams of the Pearl River Talent Recruitment Program (2019ZT08X340).

Disclosures. The authors declare no conflicts of interest.

Data Availability. The data are available from the authors upon reasonable request.

REFERENCES

1. K. Y. Bliokh, E. Karimi, M. J. Padgett, *et al.*, "Roadmap on structured waves," J. Opt. **25**, 103001 (2023).
2. B. Heinrich, M. Rastei, D.-J. Choi, *et al.*, "Engineering negative differential conductance with the Cu (111) surface state," Phys. Rev. Lett. **107**, 246801 (2011).
3. S. Brûlé, E. Javelaud, S. Enoch, *et al.*, "Experiments on seismic metamaterials: molding surface waves," Phys. Rev. Lett. **112**, 133901 (2014).
4. T. Zentgraf, Y. Liu, M. H. Mikkelsen, *et al.*, "Plasmonic Luneburg and Eaton lenses," Nat. Nanotechnol. **6**, 151–155 (2011).
5. J. Lin, J. P. B. Mueller, Q. Wang, *et al.*, "Polarization-controlled tunable directional coupling of surface," Science **340**, 331–334 (2013).
6. B. Yang, Q. Guo, B. Tremain, *et al.*, "Ideal Weyl points and helicoid surface states in artificial photonic crystal structures," Science **359**, 1013–1016 (2018).
7. B. Yang, Q. Guo, D. Wang, *et al.*, "Scalar topological photonic nested meta-crystals and skyrmion surface states in the light cone continuum," Nat. Mater. **22**, 1203–1209 (2023).
8. I. Garca-Elcano, J. Merino, J. Bravo-Abad, *et al.*, "Probing and harnessing photonic Fermi arc surface states using light-matter interactions," Sci. Adv. **9**, eadf8257 (2023).
9. X. Wang, M. S. Mirmoosa, V. S. Asadchy, *et al.*, "Metasurface-based realization of photonic time crystals," Sci. Adv. **9**, eadg7541 (2023).
10. Y.-F. Cheng, X. Ding, F. Peng, *et al.*, "Broadband dual-, triple-, and quad-resonance endfire antennas based on surface waves," IEEE Trans. Antennas Propag. **68**, 6389–6394 (2020).
11. A. Shojaeifard, K.-K. Wong, K.-F. Tong, *et al.*, "MIMO evolution beyond 5G through reconfigurable intelligent surfaces and fluid antenna systems," Proc. IEEE **110**, 1244–1265 (2022).
12. K. Ishizaki and S. Noda, "Manipulation of photons at the surface of three-dimensional photonic crystals," Nature **460**, 367–370 (2009).
13. L. Lu, J. D. Joannopoulos, M. Soljačić, *et al.*, "Waveguiding at the edge of a three-dimensional photonic crystal," Phys. Rev. Lett. **108**, 243901 (2012).
14. K. Luo, Z. Huang, X. Lv, *et al.*, "Directional Bloch surface wave coupling enabled by magnetic spin-momentum locking of light," Nanoscale Adv. **5**, 1664–1671 (2023).
15. M. Wang, H. Zhang, T. Kovalevich, *et al.*, "Magnetic spin–orbit interaction of light," Light Sci. Appl. **7**, 24 (2018).
16. Y.-C. Lee, Y.-L. Ho, B.-W. Lin, *et al.*, "High-*Q* lasing via all-dielectric Bloch-surface-wave platform," Nat. Commun. **14**, 6458 (2023).
17. Z. Zhang, Z. Wang, C. Zhang, *et al.*, "Advanced terahertz refractive sensing and fingerprint recognition through metasurface-excited surface waves," Adv. Mater. **36**, 2308453 (2024).
18. M. Z. Hasan and C. L. Kane, "Colloquium: topological insulators," Rev. Mod. Phys. **82**, 3045–3067 (2010).
19. L. Lu, J. D. Joannopoulos, and M. Soljačić, "Topological photonics," Nat. Photonics **8**, 821–829 (2014).
20. Z. Wang, Y. Chong, J. D. Joannopoulos, *et al.*, "Observation of unidirectional backscattering-immune topological electromagnetic states," Nature **461**, 772–775 (2009).
21. K. Fang, Z. Yu, and S. Fan, "Realizing effective magnetic field for photons by controlling the phase of dynamic modulation," Nat. Photonics **6**, 782–787 (2012).
22. L.-H. Wu and X. Hu, "Scheme for achieving a topological photonic crystal by using dielectric material," Phys. Rev. Lett. **114**, 223901 (2015).
23. W. Zhang, H. Yuan, N. Sun, *et al.*, "Observation of novel topological states in hyperbolic lattices," Nat. Commun. **13**, 2937 (2022).
24. M. Jung, R. G. Gladstone, and G. Shvets, "Nanopolaritonic second-order topological insulator based on graphene plasmons," Adv. Photon. **2**, 046003 (2020).
25. T. Ma and G. Shvets, "All-Si valley-Hall photonic topological insulator," New J. Phys. **18**, 025012 (2016).
26. J.-W. Dong, X.-D. Chen, H. Zhu, *et al.*, "Valley photonic crystals for control of spin and topology," Nat. Mater. **16**, 298–302 (2017).
27. X.-D. Chen, F.-L. Zhao, M. Chen, *et al.*, "Valley-contrasting physics in all-dielectric photonic crystals: orbital angular momentum and topological propagation," Phys. Rev. B **96**, 020202 (2017).
28. X. Wu, Y. Meng, J. Tian, *et al.*, "Direct observation of valley-polarized topological edge states in designer surface plasmon crystals," Nat. Commun. **8**, 1304 (2017).
29. J. Noh, S. Huang, K. P. Chen, *et al.*, "Observation of photonic topological valley Hall edge states," Phys. Rev. Lett. **120**, 063902 (2018).
30. Y. Kang, X. Ni, X. Cheng, *et al.*, "Pseudo-spin–valley coupled edge states in a photonic topological insulator," Nat. Commun. **9**, 3029 (2018).
31. F. Gao, H. Xue, Z. Yang, *et al.*, "Topologically protected refraction of robust kink states in valley photonic crystals," Nat. Phys. **14**, 140–144 (2018).
32. C. A. Rosiek, G. Arregui, A. Vladimirova, *et al.*, "Observation of strong backscattering in valley-hall photonic topological interface modes," Nat. Photonics **17**, 386–392 (2023).
33. X. Xie, S. Yan, J. Dang, *et al.*, "Topological cavity based on slow-light topological edge mode for broadband Purcell enhancement," Phys. Rev. Appl. **16**, 014036 (2021).
34. X.-T. He, E.-T. Liang, J.-J. Yuan, *et al.*, "A silicon-on-insulator slab for topological valley transport," Nat. Commun. **10**, 872 (2019).
35. H. Chu, Z.-G. Chen, Y. Lai, *et al.*, "Wave steering by relaying interface states in a valley-Hall-derived photonic superlattice," Phys. Rev. Appl. **16**, 044006 (2021).
36. Y. Shen, B. Yu, H. Wu, *et al.*, "Topological transformation and free-space transport of photonic hopfions," Adv. Photon. **5**, 015001 (2023).
37. Z. Guo, X. Wu, Y. Sun, *et al.*, "Anomalous broadband Floquet topological metasurface with pure site rings," Adv. Photon. Nexus **2**, 016006 (2023).
38. H. Wang, G. Tang, Y. He, *et al.*, "Ultracompact topological photonic switch based on valley-vortex-enhanced high-efficiency phase shift," Light Sci. Appl. **11**, 292 (2022).
39. Y. Zeng, U. Chattopadhyay, B. Zhu, *et al.*, "Electrically pumped topological laser with valley edge modes," Nature **578**, 246–250 (2020).
40. Z.-K. Shao, H.-Z. Chen, S. Wang, *et al.*, "A high-performance topological bulk laser based on band-inversion-induced reflection," Nat. Nanotechnol. **15**, 67–72 (2020).
41. W. Liu, Z. Ji, Y. Wang, *et al.*, "Generation of helical topological exciton-polaritons," Science **370**, 600–604 (2020).
42. Y. Yang, Y. Yamagami, X. Yu, *et al.*, "Terahertz topological photonics for on-chip communication," Nat. Photonics **14**, 446–451 (2020).
43. R. Jia, S. Kumar, T. C. Tan, *et al.*, "Valley-conserved topological integrated antenna for 100-Gbps THz 6G wireless," Sci. Adv. **9**, eadi8500 (2023).
44. S. Barik, A. Karasahin, S. Mittal, *et al.*, "Chiral quantum optics using a topological resonator," Phys. Rev. B **101**, 205303 (2020).
45. M. J. Mehrabad, A. P. Foster, R. Dost, *et al.*, "Chiral topological photonics with an embedded quantum emitter," Optica **7**, 1690–1696 (2020).

46. Z. Lan, J. W. You, Q. Ren, *et al.*, "Second-harmonic generation via double topological valley-Hall kink modes in all-dielectric photonic crystals," Phys. Rev. A **103**, L041502 (2021).
47. H. Zhong, S. Xia, Y. Zhang, *et al.*, "Nonlinear topological valley Hall edge states arising from type-II Dirac cones," Adv. Photon. **3**, 056001 (2021).
48. D. Smirnova, D. Leykam, Y. Chong, *et al.*, "Nonlinear topological photonics," Appl. Phys. Rev. **7**, 021306 (2020).
49. W. A. Benalcazar, B. A. Bernevig, and T. L. Hughes, "Quantized electric multipole insulators," Science **357**, 61–66 (2017).
50. Y. Zhang, D. Bongiovanni, Z. Wang, *et al.*, "Realization of photonic p-orbital higher-order topological insulators," eLight **3**, 5 (2023).
51. G. Harari, M. A. Bandres, Y. Lumer, *et al.*, "Topological insulator laser: theory," Science **359**, eaar4003 (2018).
52. J. Chen, W. Liang, and Z.-Y. Li, "Strong coupling of topological edge states enabling group-dispersionless slow light in magneto-optical photonic crystals," Phys. Rev. B **99**, 014103 (2019).
53. G. Arregui, J. Gomis-Bresco, C. M. Sotomayor-Torres, *et al.*, "Quantifying the robustness of topological slow light," Phys. Rev. Lett. **126**, 027403 (2021).
54. F.-F. Li, H.-X. Wang, Z. Xiong, *et al.*, "Topological light-trapping on a dislocation," Nat. Commun. **9**, 2462 (2018).
55. C. Lu, C. Wang, M. Xiao, *et al.*, "Topological rainbow concentrator based on synthetic dimension," Phys. Rev. Lett. **126**, 113902 (2021).
56. C. Lu, Y.-Z. Sun, C. Wang, *et al.*, "On-chip nanophotonic topological rainbow," Nat. Commun. **13**, 2586 (2022).
57. X. Xi, J. Ma, S. Wan, *et al.*, "Observation of chiral edge states in gapped nanomechanical graphene," Sci. Adv. **7**, eabe1398 (2021).
58. R. Xi, Q. Chen, Q. Yan, *et al.*, "Topological chiral edge states in deep-subwavelength valley photonic metamaterials," Laser Photon. Rev. **16**, 2200194 (2022).
59. Z. Zhang, Z. Lan, Y. Xie, *et al.*, "Bound topological edge state in the continuum for all-dielectric photonic crystals," Phys. Rev. Appl. **16**, 064036 (2021).
60. Y. Feng, Z. Zhang, F. Qin, *et al.*, "Bound valley edge states in the continuum," Opt. Lett. **47**, 3107–3110 (2022).
61. K. Qu, K. Chen, Q. Hu, *et al.*, "Deep-learning-assisted inverse design of dual-spin/frequency metasurface for quad-channel off-axis vortices multiplexing," Adv. Photon. Nexus **2**, 016010 (2023).
62. H. S. Nguyen, F. Dubois, T. Deschamps, *et al.*, "Symmetry breaking in photonic crystals: on-demand dispersion from flatband to Dirac cones," Phys. Rev. Lett. **120**, 066102 (2018).
63. J. Stein, H.-J. Stöckmann, and U. Stoffregen, "Microwave studies of billiard Green functions and propagators," Phys. Rev. Lett. **75**, 53–56 (1995).